nature communications

Article

https://doi.org/10.1038/s41467-024-52520-1

Cohesive energy discrepancy drives the fabrication of multimetallic atomically dispersed materials for hydrogen evolution reaction

Received: 30 December 2023

Accepted: 11 September 2024

Xinyi Yang[1], Wanqing Song[1], Kang Liao[1], Xiaoyang Wang[1], Xin Wang[1], Jinfeng Zhang[1], Haozhi Wang[1,2], Yanan Chen[1], Ning Yan[3], Xiaopeng Han[1,4] ✉, Jia Ding[1,4] ✉ & Wenbin Hu[1,2,4]

Atomically dispersed single atom (SA) and atomic cluster (AC) metallic materials attract tremendous attentions in various fields. Expanding monometallic SA and AC to multimetallic SA/AC composites opens vast scientific and technological potentials yet exponentially increasing the synthesis difficulty. Here, we present a general energy-selective-clustering methodology to build the largest reported library of carbon supported bi-/multi-metallic SA/AC materials. The discrepancy in cohesive energy results into selective metal clustering thereby driving the symbiosis of multimetallic SA or/and AC. The library includes 23 bimetallic SA/AC composites, and expanded compositional space of 17 trimetallic, quinary-metallic, septenary-metallic SA/AC composites. We chose bimetallic $M^1_{SA}M^2_{AC}$ to demonstrate the electrocatalysis utility. Unique decoupled active sites and inter-site synergy lead to 8/47 mV overpotential at 10 mA cm^{-2} for alkaline/acidic hydrogen evolution and over 1000 h durability in water electrolyzer. Moreover, delicate modulations towards composition and configuration yield high-performance catalysts for multiple electrocatalysis systems. Our work broadens the family of atomically dispersed materials from monometallic to multimetallic and provides a platform to explore the complex composition induced unconventional effects.

Atomically dispersed metallic materials are of significant interests in various applications because of the maximum atom-utilization efficiency, unique electronic structure and tunable coordination environment[1–4]. Multimetallic, multi-scale atomic materials comprising multiple types of single atom (SA) or/and atomic cluster (AC) species, such as bimetallic dual-atom, medium-/high-entropy SA and heterogeneous SA-AC composites, can significantly expand the scientific and application potentials beyond the horizons of monometallic counterparts[5–7]. In recent years, strategies like metal-organic framework pyrolysis[8,9], atomic layer deposition[10,11] and atom self-assembly[12–14] etc. were developed for synthesizing multimetallic atomically dispersed materials, which are of pivotal significance in chemical (e.g. electrocatalysis[9,15], thermocatalysis[16,17], organic synthesis[18,19]), physical (e.g. magnetics[20], optics[21,22], electronics[23]) and environmental (e.g. water treatment[24,25], plastic degradation[26]) application areas.

---

[1]School of Materials Science and Engineering, Tianjin University, Tianjin, China. [2]Joint School of National University of Singapore and Tianjin University, International Campus of Tianjin University, Fuzhou, China. [3]School of Physics and Technology, Wuhan University, Wuhan, China. [4]National Industry-Education Platform of Energy Storage, Tianjin University, Tianjin, China. ✉e-mail: xphan@tju.edu.cn; jiading@tju.edu.cn

Despite the recent surge of researches on multimetallic SA/AC composite based materials, significantly challenges still remain. First, simultaneously constructing high free-energy multimetallic SA and AC raises higher difficulty as compared to simply stabilizing monotype SA or AC moiety[27,28]. Apart from some highly sophisticated methodology[29], in most cases the principles of synthesizing monometallic SA/AC cannot be extrapolated to another metal element. Previous studies routinely employed specie-by-specie synthesis processes for respectively fabricating each specie[9,30,31], which are cumbersome and non-universal. Second, as higher multimetallic compositional space opened (i.e. ≥3 metal elements), the difficulties for precise and controllable synthesis increase exponentially. Currently there is a knowledge gap in how to integrate numerous SA or/and AC species of different elements and varied physical/chemical properties on one solid substrate. Third, the inherent synergy between symbiotic adjacent metal species in multimetallic SA/AC composite is of vital importance in determining the apparent functionality. The controllable method of creating intrinsic interaction among diverse multimetallic SA/AC is highly desired yet there is still no such a precedent in previous studies. Therefore, developing an efficient and general synthesis strategy for multimetallic SA/AC composite is urgently demanded and could bring a new repertoire of structure-property mechanisms and potential capabilities.

Hydrogen with merits of high mass energy density and cleanness is an ideal energy carrier to address global fossil energy shortage and environmental challenges. Electrocatalytic hydrogen evolution powered by renewable electricity is recognized as an eco-friendly way to produce green hydrogen[32,33]. Noble metals deliver attractive electrocatalytic activity and durability towards hydrogen evolution reaction (HER) yet suffer from low abundance and high costs. Therefore, the concept of multimetallic atomically dispersed material is highly promising for fabricating high-performance hydrogen electrocatalysts with minimal noble metal usage[34–36].

Herein, we developed a general energy-selective-clustering methodology to fabricate a large library of carbon supported bi-/multi-metallic SA/AC materials. Driven by the discrepancy in cohesive energy of metals, various metal ions exhibit differentiated clustering tendencies on a nitrogen functionalized carbon nanobox (NCB) thereby achieving the symbiosis of multimetallic single atoms or/and atomic clusters with native inter-site interaction. A library comprising 23 types of bimetallic SA/AC composites, and 17 types of trimetallic, quinary-metallic, septenary-metallic SA/AC composites was fabricated involving 17 metal elements. Bimetallic $M_{SA}Ru_{AC}$ (M = Fe/Co/Ni) were selected to demonstrate the high value of the library for hydrogen electrocatalysis utility. Moreover, through general composition modification, high-performance catalysts of $Fe_{SA}Pt_{AC}$ and $Cr_{SA}Ir_{AC}$ were efficiently developed for oxygen reduction and evolution reaction electrocatalysis, respectively. Our work will open new space for fabricating multimetallic atomically dispersed materials with significant potential for a wide range of applications.

Results

Mechanism of the energy-selective-clustering methodology

The formation process of metallic atomic aggregates (AA) from isolated metal precursors on a solid substrate is demonstrated in Fig. 1a. Essentially, the clustering of isolated metal atoms is dominated by the inherent metal cohesion and metal-support interaction (MSI)[37–39]. From the perspective of thermodynamics, the driving force of clustering is the cohesive energy (E_c) due to the lower free energy of aggregated bulk metal than that of isolated metal atoms. The resistance of clustering is the metal-substrate binding energy (E_b) because an isolated metal atom needs to overcome E_b for escaping from the original location before it can couple with another individual atom or incorporate into a multi-atom cluster[40]. Therefore, the clustering tendency of metal atoms is determined by cohesive energy and the binding energy ($\Delta E = E_c - E_b$)[41–43]. As demonstrated in Fig. 1a, considering two elements of isolated metal atoms (M^1, M^2) on one substrate, the high temperature sintering can induce the metal with higher clustering tendency to form atomic cluster (AC). Simultaneously, the metal with lower cluster tendency would form more stable single atom (SA) species.

Based on this energy controlled selective clustering process, it is feasible to fabricate bimetallic composite of $M^1{}_{SA}$-$M^2{}_{SA}$, $M^1{}_{SA}$-$M^2{}_{AC}$ or $M^1{}_{AC}$-$M^2{}_{AC}$ by exploiting the different clustering tendencies of metals. Bimetallic pair of Ni and Ru was chosen to verified this principle. The substrate employed is a nitrogen functionalized carbon nanobox (NCB) prepared by chemical vapor deposition method (Fig. S1). NCB is selected on account of the robust cube morphology (Fig. S2a), which provide spacious substrates to load metal atoms and exert minimum geometric shielding on the metal ripening. Besides, NCB possesses unique graphitic tissue and surface chemistry. The NCB shells are built by long parallel graphene multilayers (Fig. S2b), suggesting the high graphitization degree and favorable electronic conductivity. The analyses of nitrogen structures on NCB surface are demonstrated in Fig. S3.

The precursor for sintering is prepared by room temperature wet-impregnation method, during which process NCB was immersed into Ni/Ru salt solutions for adsorbing the hydrated Ni/Ru ions. This scenario is demonstrated by the schematic in Fig. S4. Density functional theory (DFT) calculations were conducted to evaluate the clustering tendency of adsorbed Ru and Ni ions on NCB. First, the cohesive energies (E_c) for Ru and Ni are calculated to be −7.021 eV and −4.788 eV, respectively. Regarding to the binding energy (E_b), due to the solvation structures of hydrated Ni/Ru ions, the metal ions cannot form direct covalent bonds to the substrate therefore the adsorption of hydrated Ni/Ru ions on NCB should be weak. As expected, the calculated binding energies (E_b) are −0.754 eV and −0.680 eV for Ru and Ni, and the E_b values corresponding to three types of nitrogen modified substrates in NCB are very close (Fig. S5). Basically, the absolute values of E_b are much lower than E_c for Ru and Ni, therefore the clustering tendency of Ni/Ru ions should be dominated by the cohesive energy. On this basis, Ru has higher clustering tendency than Ni due to the much larger cohesive energy. The discrepancy in E_c will result in the selective clustering of Ru and the formation of $Ni_{SA}Ru_{AC}$ composite on NCB. This mechanism is validated by the following comprehensive experimental results.

As shown in Fig. 1b, high-angle annular dark-field scanning transmission electron microscopy (HAADF-STEM) image and corresponding energy dispersive X-ray spectroscopy (EDS) mapping prove the isolated atom configuration of Ni/Ru in the precursor (25 °C). Intriguingly, Ni and Ru demonstrated different clustering behaviors in the following sintering. At 100 °C, Ru atoms agglomerated into sub-nanometer atomic clusters (Ru_{AC}). On the contrary, Ni atoms formed stable single atom species (Ni_{SA}). The higher temperature of 300 °C and 500 °C further increased the Ru_{AC} size yet still cannot induce the clustering of Ni_{SA}. The EDS mapping demonstrates well-defined Ru_{AC} and monatomic Ni_{SA} uniformly distributing on NCB. Higher sintering temperatures of 600 °C and 700 °C induced further ripening of Ru_{AC} but cannot change the monatomic Fe/Co/Ni species (Figs. S6–8).

The Ni_{SA} and Ru_{AC} configurations are further verified by synchrotron extended X-ray absorption fine structure (EXAFS) spectra (Fig. 1c). Ni K-edge EXAFS spectrum displays only a pronounced nearest-neighbor peaks at ca. 1.5 Å ascribed to Ni−N bond, whereas the Ni-Ni bond is totally absent. On the contrary, Ru K-edge EXAFS spectrum displays the characteristic peak of Ru-Ru at ca. 2.4 Å, suggesting the clustering of Ru atoms into multi-atom aggregate. In-situ TEM technique was employed to further verify this selective clustering. Figure S9 displays time-series TEM images of one fixed region collected from in-situ heating TEM video (Supplementary Movie 1). With increasing temperature, isolated dark spots gradually appeared on the margins of NCBs, which can be all identified as Ru clusters by electron energy loss spectroscopy (EELS) mapping. Meanwhile, no Ni cluster or

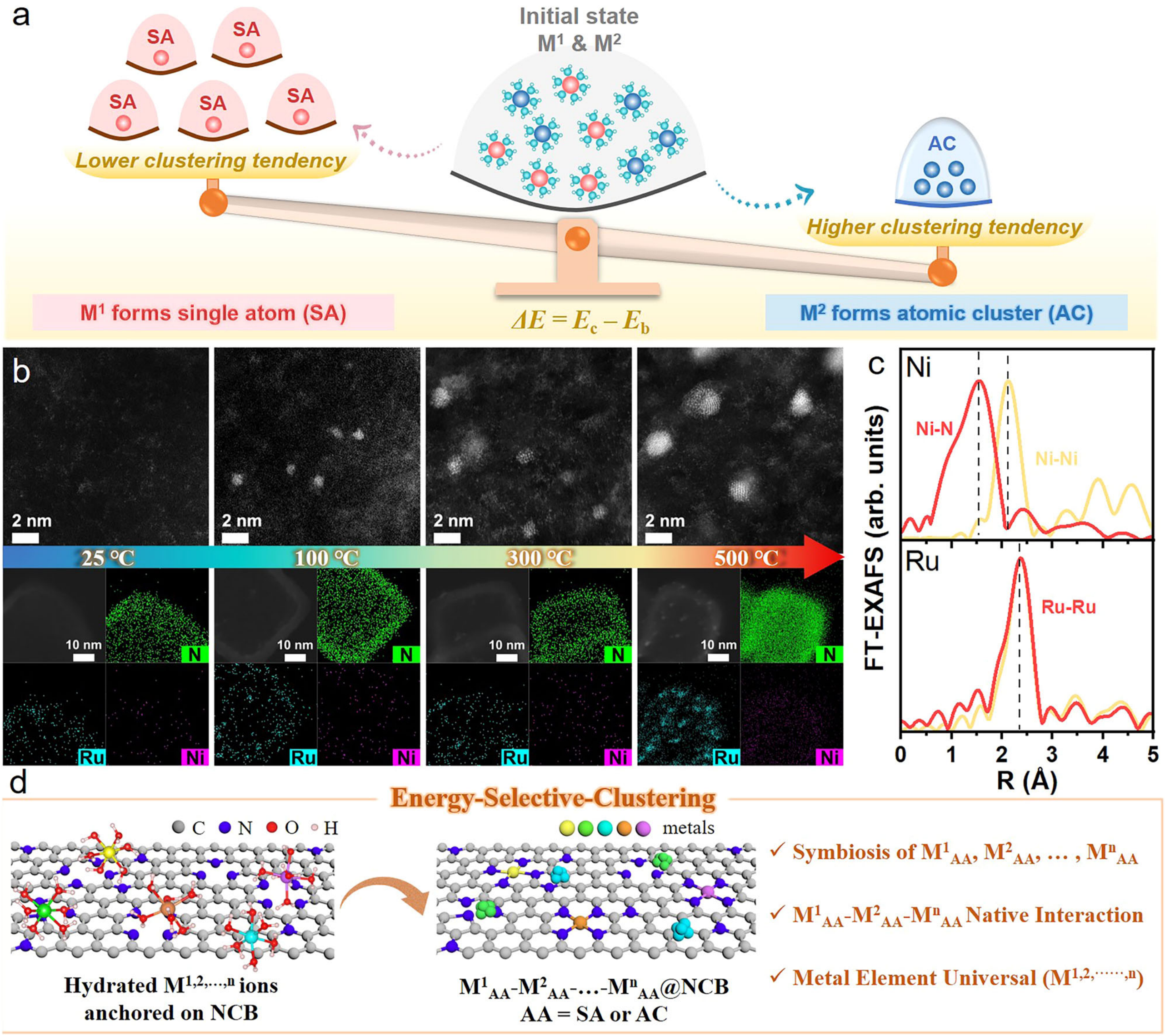

Fig. 1 | Cohesive energy controlled selective-clustering mechanism of metals. **a** Mechanism interpretation for the energy controlled clustering of two metals to respectively form SA or AC. **b** HAADF-STEM images and corresponding EDS mapping demonstrating the evolution of Ru and Ni species on NCB upon sintering. **c** The k^3-weighted Fourier transform Ni and Ru EXAFS spectra of the product (red profiles) in **b** and standard metal foils (yellow profiles). **d** Schematic of multimetallic atomic aggregate (AA = SA/AC) composites formation based on energy-selective-clustering mechanism.

particle can be observed. The locations of Ru clusters are not as uniform as those in the specimen prepared in tube furnace (Fig. S10), which is probably due to the different heating conditions in in-situ TEM specimen holder and in tube furnace. Nonetheless, the selective-clustering mechanism is still valid.

Apart from bimetallic system, we propose that the energy-selective-clustering mechanism can be expanded and be also applicable to multimetallic systems ($M^{1,2,......,n}$, $n \geq 3$). As shown in Fig. 1d, hydrated $M^{1,2,......,n}$ ions anchored on NCB can be readily prepared by wet-impregnation method. $M^{1,2,......,n}$ ions will experience different ripening processes due to the different clustering tendencies, which are in thermodynamics determined by the cohesive energy (E_c) and binding energy (E_b)[43,44]. In addition to Ni/Ru, we investigated the other various metal elements in terms of cohesive energy, adsorption configuration and corresponding adsorption energies. As shown in Fig. S11, due to the water solvation effects, the interactions between hydrated metal ions and NCB are in the level of weak physical adsorption (E_b = ~ 0.7 eV)[45,46]. More importantly, because the central metal ions were largely shielded by the solvation shell, the E_b values for different metals are quite close (σ^2 (E_b) = 0.006 eV^2). By contrast, the absolute values of cohesive energies (E_c) of these metals (Table S1) are much higher than E_b, and discrepancy among different metals is also much more pronounced (σ^2 (E_c) = 3.148 eV^2). Therefore, the clustering tendency of $M^{1,2,......,n}$ on NCB is essentially dominated by their corresponding cohesive energies (E_c). Due to the discrepancy in cohesive energy, different metal ions will exhibit selective-clustering upon sintering and the symbiosis of multimetallic atomic aggregates (M^1_{AA}-M^2_{AA}-...-M^n_{AA}, AA = SA or AC) can be achieved. The symbiotic multimetallic AAs are spatially adjacent, which will probably induce strong native interaction and synergistic effect.

Synthesis and characterization of bi-/multi-metallic SA/AC composite library

Figure 2a is a cohesive energy based element periodic table displaying the absolute values of cohesive energy in the vertical axis[47]. Since the clustering tendency of hydrated metal ions on NCB is dominated by cohesive energy, guided by this element periodic table, we utilize the energy-selective-clustering methodology to fabricate a library of NCB

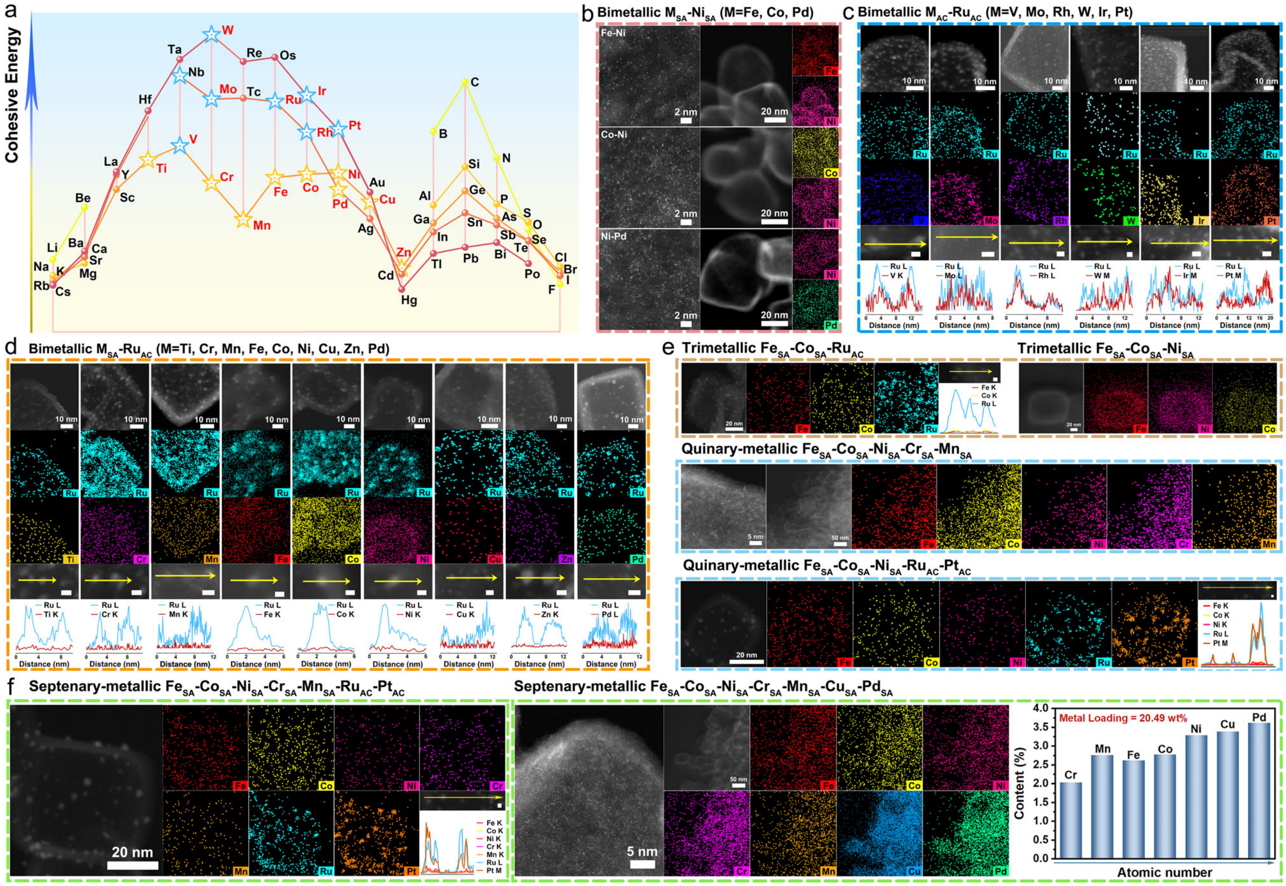

Fig. 2 | Synthesis and characterization of bi-/multi-metallic SA/AC composites. **a** Element periodic table based on cohesive energy values. HAADF-STEM, and EDS mapping/line scans of **b** bimetallic SA-SA composites, **c** bimetallic AC-AC composites and **d** bimetallic SA-AC composites based on different metal element pairs. HAADF-STEM, EDS mapping/line scans of **e** trimetallic SA/AC, quinary-metallic SA/AC, and **f** representative septenary-metallic SA/AC composites. Unmarked scale bars are 2 nm.

supported bi-/multi-metallic SA/AC composites (Table S2). For the bimetallic systems, we selected 18 bimetallic pairs ascribed to three categories: i) three M^1-M^2 bimetallic pairs with cohesive energies both lower than Ru (Fe-Ni, Co-Ni, Ni-Pd pairs); ii) nine M-Ru bimetallic pairs with cohesive energies of M lower than Ru (M = Ti, Cr, Mn, Fe, Co, Ni, Cu, Zn, Pd); iii) six M-Ru bimetallic pairs with cohesive energy of M higher than Ru (M = V, Mo, Rh, W, Ir, Pt). Sintering conditions were kept identical in order to achieve rigorous side-by-side comparison. Figure 2b–d show the HAADF-STEM, and EDS mapping/line scans of the obtained bimetallic SA/AC composites. For the three type-i M^1-M^2 bimetallic pairs, no metallic AC or nanoparticles can be observed in HAADF-STEM images. The metals exist as single atoms on NCB. The EDS mappings demonstrate the uniform distribution of Fe, Co, Ni, Pd elements. Therefore, dual-single-atom composites of Fe_{SA}-Ni_{SA}, Co_{SA}-Ni_{SA}, Ni_{SA}-Pd_{SA} were obtained (Fig. 2b). For nine type-ii M-Ru bimetal pairs, clear Ru clusters can be observed both in HAADF-STEM images and EDS mappings for all specimens. On the contrary, the Ti, Cr, Mn, Fe, Co, Ni, Cu, Zn, Pd elements with lower cohesive energy display no clue of clustering. Therefore, composites of M_{SA}-Ru_{AC} were prepared. For six type-iii M-Ru bimetallic pairs, atomic clusters of both M element and Ru appear for all the samples. The adjacent M_{AC} and Ru_{AC} can be clearly detected by the EDS line scans, indicating the construction of six types of M_{AC}-Ru_{AC} composites (Fig. 2c). To further demonstrate the synthesis generality, five more Ru-free bimetallic materials (Mn_{SA}-Pt_{AC}, Cr_{SA}-Rh_{AC}, Fe_{SA}-W_{AC}, Co_{SA}-Mo_{AC}, Ni_{SA}-Nb_{AC}) were also fabricated (Fig. S12).

By virtue of the generality for multimetallic system, the energy-selective-clustering based synthesis methodology is also applicable to the construction of trimetallic and medium/high-entropy multi-metallic SA/AC composites. Figures 2e, f and S13 demonstrate the as-synthesized trimetallic, quinary-metallic and septenary-metallic SA/AC composites. Employing relatively low cohesive energy metals, trimetallic and quinary-metallic single atom materials including Fe_{SA}-Co_{SA}-Ni_{SA} and Fe_{SA}-Co_{SA}-Ni_{SA}-Cr_{SA}-Mn_{SA} were fabricated, as proved by the HAADF-STEM images. As metals with relatively higher cohesive energy were added, trimetallic and quinary-metallic SA-AC composites (e.g. Fe_{SA}-Co_{SA}-Ru_{AC} and Fe_{SA}-Co_{SA}-Ni_{SA}-Ru_{AC}-Pt_{AC}) can be obtained. The EDS line scans on randomly selected bright clusters recognized the Ru_{AC} and Pt_{AC}. In our study, the energy-selective-clustering method can efficiently synthesize high-entropy septenary-metallic single atom material, e.g. Fe_{SA}-Co_{SA}-Ni_{SA}-Cr_{SA}-Mn_{SA}-Cu_{SA}-Pd_{SA}. The loading of each metal is fairly high leading to the total loading of 20.49 wt% (Table S3), which is the highest loading of high-entropy single atom materials reported to date[2,48,49]. The synthesis of high-entropy single atom materials is highly challenging thus rarely reported. Analogue to tri-metallic and quinary-metallic counterparts, septenary-metallic SA-AC composites (e.g. Fe_{SA}-Co_{SA}-Ni_{SA}-Cr_{SA}-Mn_{SA}-Ru_{AC}-Pt_{AC}, Zn_{SA}-Fe_{SA}-Cr_{SA}-Ti_{SA}-Mn_{SA}-Ir_{AC}-V_{AC}, Zn_{SA}-Fe_{SA}-Co_{SA}-Ti_{SA}-Ni_{SA}-Nb_{AC}-W_{AC} and Pt_{AC}-V_{AC}-Ru_{AC}-Mo_{AC}-Nb_{AC}-Ir_{AC}-Rh_{AC}) can be obtained by adopting high cohesive energy metals. Therefore, our method provides an excellent platform for studying atomically dispersed multimetallic SA/AC materials with tunable configurational mixing entropy.

We conducted comprehensive characterizations on the aforementioned materials. The metal elements and corresponding atomic configurations in all the as-synthesized bi-/multi-metallic SA/AC materials are summarized in Fig. 3a, which clearly demonstrates the

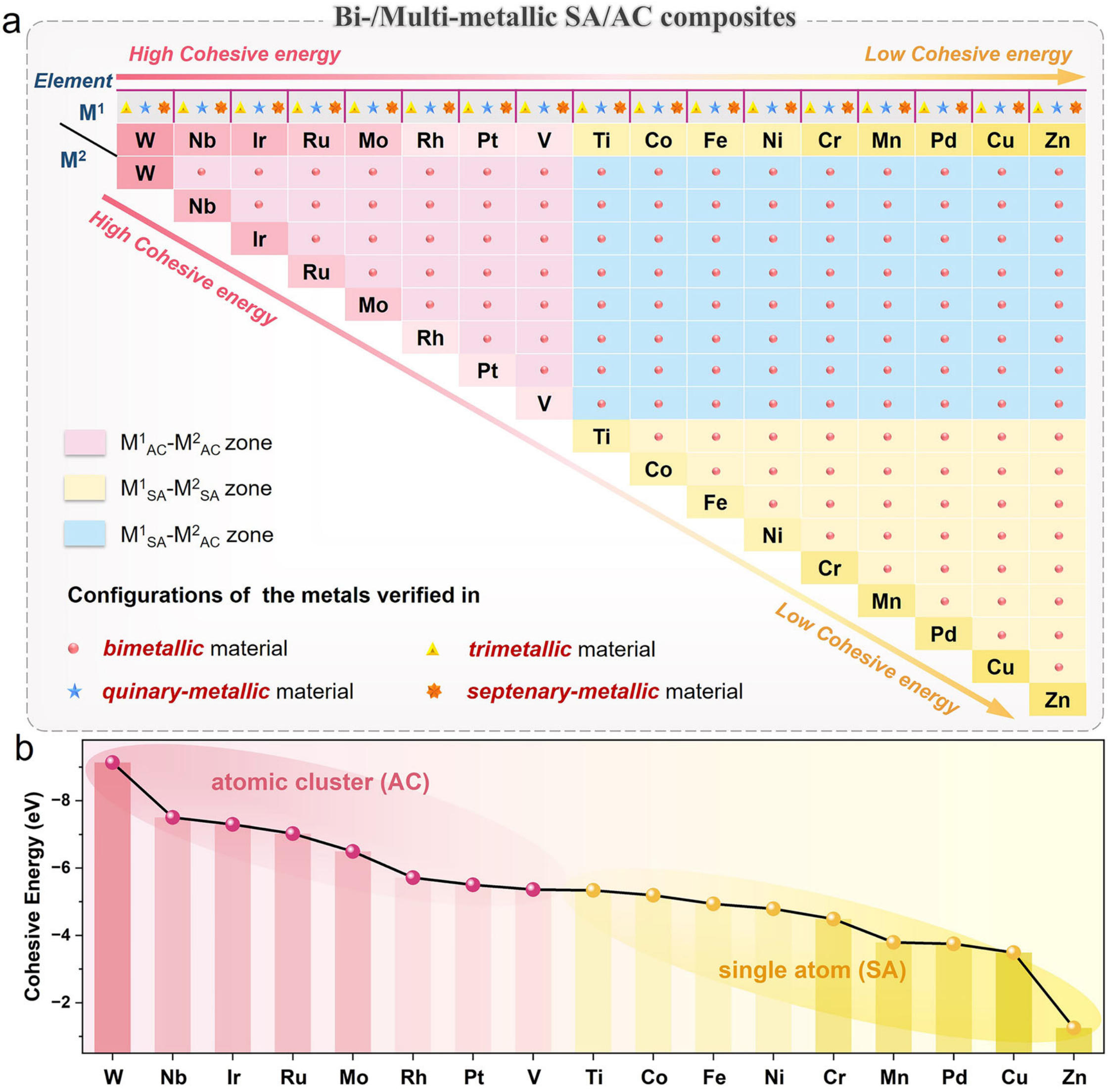

Fig. 3 | Correlation between cohesive energy and atomic configurations of various metal elements. a The summary of as-synthesized atomically dispersed bimetallic and multimetallic materials. **b** The cohesive energies of the metal elements involved in the synthesis and the corresponding SA or AC configuration in the obtained bi-/multi-metallic materials.

underlying correlation between atomic configuration and the cohesive energy of metals. According to the atomic configurations of these elements in bimetallic materials, the M^1_{AC}-M^2_{AC}, M^1_{SA}-M^2_{SA}, M^1_{SA}-M^2_{AC} zones can be defined, which are in strict conformity with the relevant values of cohesive energy. Apart from bimetallic materials, the atomic configurations of 17 metal elements can be further verified in trimetallic, quinary-metallic, septenary-metallic materials, as indicated by the marks of triangle, pentagram and heptagram in Fig. 3a. For instance, regarding the Fe-Pt pair in the M^1_{SA}-M^2_{AC} zone, the configurations of Fe and Pt are verified as Fe_{SA} and Pt_{AC} in bimetallic, trimetallic, quinary-metallic and septenary-metallic materials. Overall, for the 17 elements involved (Fig. S14), based on the NCB substrate and current synthesis conditions, the metal elements with relatively lower cohesive energies (Ti, Co, Fe, Ni, Cr, Mn, Pd, Cu, Zn) formed stable SA, and the metal elements with relatively higher cohesive energies (V, Pt, Rh, Mo, Ru, Ir, Nb, W) underwent various extents of clustering and yielded AC, as displayed in Fig. 3b. Therefore, the general principle can be extracted that the clustering tendency of metal on NCB substrate demonstrates well-defined positive correlation with the cohesive energy.

Essentially different from the previous studies, our methodology for the first time validates the controllable design and synthesis of atomically precise bi-/multi-metallic materials guided by the correlation between target atomic configuration and inherent energy character of metals. This approach demonstrated excellent element and configuration generality. Moreover, through the modulation of synthetic factors including carbon substrate traits and the sintering conditions, the boundary between SA elements and AC elements could be effectively adjusted thereby further expanding the composition and configuration spaces of atomically dispersed multimetallic materials.

Fine structures of representative bimetallic (Fe_{SA}/Co_{SA}/Ni_{SA}) Ru_{AC} materials

Bimetallic $M_{SA}Ru_{AC}$@NCB (M = Fe, Co, Ni) were selected for understanding the fine structures and electrocatalysis utility of bi-/multi-metallic SA/AC composite library. The HAADF-STEM images (Fig. 4a) and EDS line scans (Fig. S15) verified the coexistence of Ru_{AC} and isolated $(Fe/Co/Ni)_{SA}$. The atomic mappings in Fig. 4a visually demonstrate the distributions of Ru clusters and monatomic Fe/Co/Ni, as well as the spatial overlapping of Ru_{AC} and Fe_{SA}/Co_{SA}/Ni_{SA} species in these materials[50,51]. To investigate the native interaction between adjacent M_{SA} and Ru_{AC}, the electronic structures were investigated by X-ray photoelectron spectroscopy (XPS). Figure 4b shows the Ru 3*p* spectra

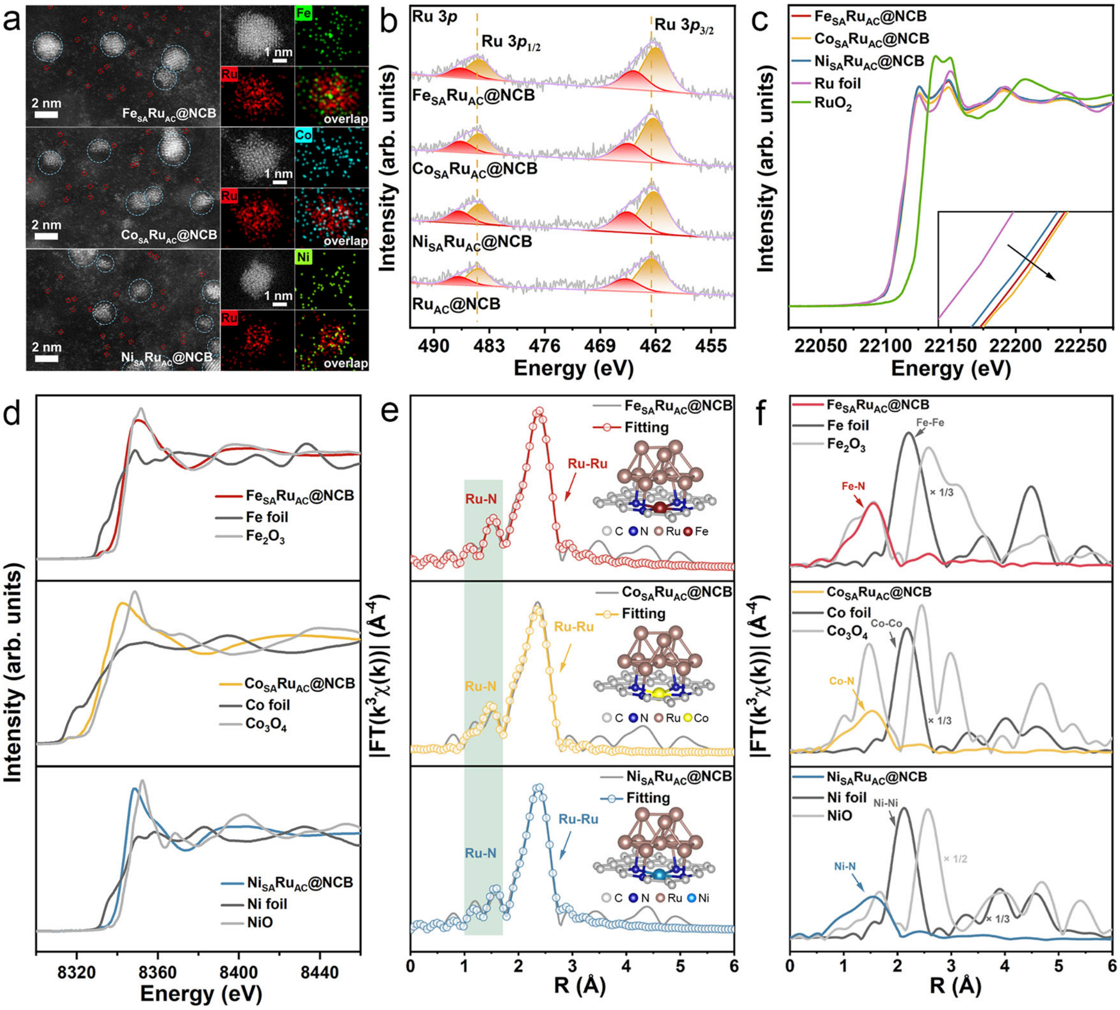

Fig. 4 | Electronic structures and atomic configurations of $M_{SA}Ru_{AC}$@NCB. **a** HAADF-STEM images and atomic mapping of $Fe_{SA}Ru_{AC}$@NCB, $Co_{SA}Ru_{AC}$@NCB and $Ni_{SA}Ru_{AC}$@NCB. **b** High-resolution XPS spectra of Ru 3*p* for $M_{SA}Ru_{AC}$@NCB and Ru_{AC}@NCB. **c** The normalized Ru K-edge XANES spectra and **e** the k^3-weighted Fourier transform EXAFS spectra of $M_{SA}Ru_{AC}$@NCB and the references. Insets: models for spectra fitting. **d** The normalized Fe/Co/Ni K-edge XANES spectra and **f** the k^3-weighted Fourier transform EXAFS spectra in *R* space of $M_{SA}Ru_{AC}$@NCB and the references.

with spin-orbit split Ru $3p_{3/2}$ and Ru $3p_{1/2}$ peaks. Compared to M_{SA} free Ru_{AC}@NCB, the Ru 3*p* positions for $M_{SA}Ru_{AC}$@NCB display shift of around 0.3 eV to the lower binding energy, suggesting the less electron donating from Ru_{AC} to M_{SA}-modified NCB than that to M_{SA}-free NCB substrate. Different positions of Ru 3*p* indicate the different oxidation states of Ru_{AC} in $M_{SA}Ru_{AC}$@NCB, suggesting the varying degrees of interaction between Ru_{AC} and M_{SA}-modified substrates.

The electronic structures are further analyzed by X-ray absorption near edge structure (XANES) spectra. Per Fig. 4c, the pre-edge spectra of Ru in $M_{SA}Ru_{AC}$@NCB are close to Ru foil, indicating the metallic state of Ru_{AC} with enriched electron density. Moreover, the intensities of the white lines of Ru K-edge are different among $M_{SA}Ru_{AC}$@NCB, suggesting the different changes in charge density around Ru_{AC}, which is in line with the XPS results. This phenomenon reveals the intrinsic electronic interaction between the symbiotic M_{SA} and Ru_{AC} in the composites. The XANES of Fe K-edge, Co K-edge and Ni K-edge (Fig. 4d) verify the positive valence states of single atom Fe, Co and Ni in M_{SA}-N-C moieties.

The atomic configurations of $M_{SA}Ru_{AC}$ composites were resolved by synchrotron EXAFS spectra. In Fig. 4e, two characteristic peaks locate at ca. 2.4 Å and 1.5 Å being attributed to Ru-Ru and Ru-N bonding, respectively, which suggest the presence of nitrogen involved coordination environments for Ru_{AC}[52]. Wavelet transform (WT) analysis also identified the coexistence of Ru-N and Ru-Ru paths (Fig. S16). Regarding to the Fe/Co/Ni species in $M_{SA}Ru_{AC}$@NCB, the EXAFS spectra of Fe/Co/Ni in *R* space display the pronounced nearest-neighbor peaks at ca. 1.5 Å (M-N) and the absence of M-M peaks (Fig. 4f). The WT-EXAFS also display only one maximum intensity at nearly 4.5 Å^{-1} being ascribed to the M-N bond, suggesting the formation of single Fe/Co/Ni atoms (Fig. S17). Guided by the EXAFS analysis, we constructed theoretical models to simulate the real catalysts (atomic coordinates of models listed in Supplementary Data 1). We conducted comprehensive DFT calculations and ab initio molecular dynamics (AIMD) simulations to determine the most reasonable models. The detailed screening processes are demonstrated in supporting information (Figs. S18–23 and Supplementary Movies 2–19). Figure 4e insets demonstrate the adopted models after screening, which consist of 10 atoms Ru cluster (Ru_{10}) isolated by M_{SA}-N-C substrates. The EXAFS spectra of $M_{SA}Ru_{AC}$@NCB can be well fitted based on these three models (Figs. 4e, S24 and Table S4).

Hydrogen evolution performance and electrolyzer application

DFT calculations were conducted to find the potential $M^1_{SA}M^2_{AC}$ sites that could deliver high catalytic activity toward hydrogen evolution reaction (HER). Ten different $M^1_{SA}M^2_{AC}$ models were considered. As demonstrated in Figs. S25–30, $Ni_{SA}Ru_{AC}$, $Fe_{SA}Ru_{AC}$, $Co_{SA}Ru_{AC}$ were

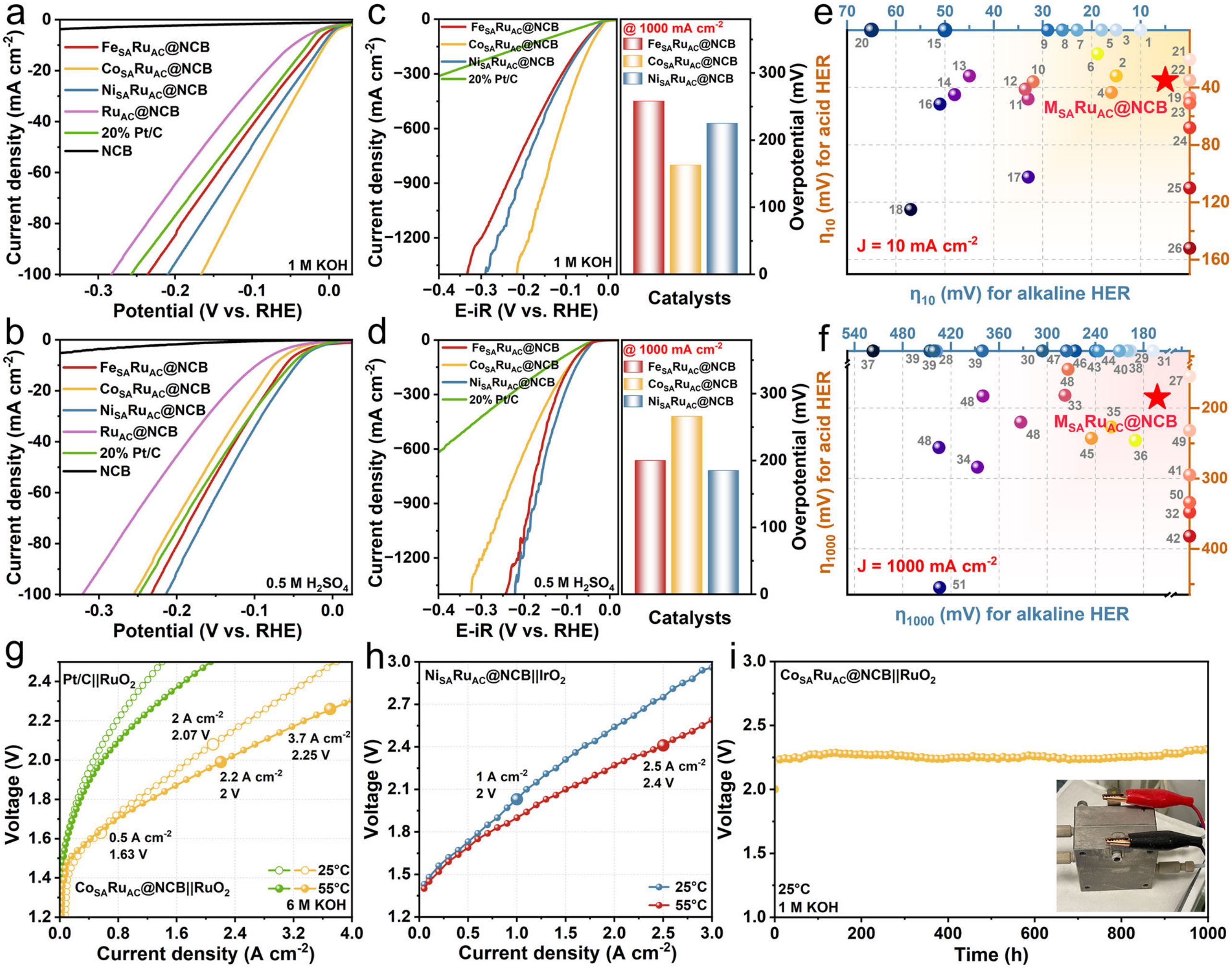

Fig. 5 | HER performance of M$_{SA}$Ru$_{AC}$@NCB and practical electrolyzer demonstration. LSV curves (non-iR corrected) of M$_{SA}$Ru$_{AC}$@NCB, Ru$_{AC}$@NCB, NCB and Pt/C in **a** 1 M KOH and **b** 0.5 M H$_2$SO$_4$. LSV curves (with 85%-iR corrected) of M$_{SA}$Ru$_{AC}$@NCB and 20% Pt/C in **c** 1 M KOH and **d** 0.5 M H$_2$SO$_4$ at industrial current density. Comparison of **e** η_{10} and **f** η_{1000} in 1 M KOH and 0.5 M H$_2$SO$_4$ for M$_{SA}$Ru$_{AC}$@NCB with the state-of-the-art HER electrocatalysts. Values were taken from references (Supplementary Tables 6 and 7). **g** Polarization curves operated at 25 °C and 55 °C of tested AWE. **h** Polarization curves of tested PEMWE operated at 25 °C and 55 °C. **i** Chronopotentiometry curve for AEM operating at 1 A cm^{-2}. Inset: photograph of the AEMWE device.

screened via theoretical energy criterion. The HER performance of as-synthesized Fe$_{SA}$/Co$_{SA}$/Ni$_{SA}$@NCB specimens were evaluated in 0.5 M H$_2$SO$_4$ and 1 M KOH electrolytes, respectively. The monometallic baselines of Ru$_{AC}$@NCB, Fe$_{SA}$/Co$_{SA}$/Ni$_{SA}$@NCB were also assessed for comparison. As shown in Fig. 5a, all M$_{SA}$Ru$_{AC}$@NCB catalysts deliver excellent electrocatalytic HER activity with ultralow overpotentials at 10 mA cm^{-2}, superior to commercial Pt/C. Pure NCB delivered negligible catalytic current, proving that the metal species contribute to the HER activity. Notably, M$_{SA}$Ru$_{AC}$@NCB exhibit alkaline HER activities in the order of Co$_{SA}$Ru$_{AC}$@NCB (8 mV) > Ni$_{SA}$Ru$_{AC}$@NCB (10 mV) > Fe$_{SA}$Ru$_{AC}$@NCB (17 mV). Both Fe$_{SA}$/Co$_{SA}$/Ni$_{SA}$@NCB and Ru$_{AC}$@NCB demonstrate much inferior HER activities than M$_{SA}$Ru$_{AC}$@NCB (Figs. 5a, S31), suggesting the underlying synergy mechanism for M$_{SA}$Ru$_{AC}$ composite in enhancing electrocatalytic performance.

The Tafel plots provide profound insight of intrinsic HER kinetic process. As shown in Fig. S32, Co$_{SA}$Ru$_{AC}$@NCB, Ni$_{SA}$Ru$_{AC}$@NCB and Fe$_{SA}$Ru$_{AC}$@NCB respectively display Tafel slope values of 20.7, 23.3 and 34.3 mV dec^{-1}, which are distinctly lower than that of Pt/C (45.2 mV dec^{-1}). The Tafel slope values indicate that the HER processes of M$_{SA}$Ru$_{AC}$@NCB comply with the Volmer-Tafel mechanism[53]. The charge transfer resistance of M$_{SA}$Ru$_{AC}$@NCB are much smaller than that of Ru$_{AC}$@NCB (Fig. S33), suggesting that the incorporation of Fe$_{SA}$/Co$_{SA}$/Ni$_{SA}$ species effectively improves the interfacial electron transfer kinetics. Co$_{SA}$Ru$_{AC}$@NCB exhibits the most facile charge transfer, which is highly conducive to the best HER activity.

For acidic HER, Ni$_{SA}$Ru$_{AC}$@NCB, Fe$_{SA}$Ru$_{AC}$@NCB and Co$_{SA}$Ru$_{AC}$@NCB demonstrate η_{10} values of 47, 61 and 75 mV (Fig. 5b). Of note, the rank in acidic HER activity for M$_{SA}$Ru$_{AC}$@NCB catalysts is different from that in alkaline HER activity, which is reflective of the different reaction mechanism under different pH conditions. All the bimetallic composite based catalysts are superior to the monometallic candidates for acidic HER (Fig. S34). The Tafel slope of Ni$_{SA}$Ru$_{AC}$@NCB is 46.1 mV dec^{-1} (Fig. S35), indicating the reaction follows the Volmer-Heyrovsky mechanism. The value is distinctly lower than those of Fe$_{SA}$Ru$_{AC}$@NCB, Co$_{SA}$Ru$_{AC}$@NCB and commercial Pt/C, suggesting the faster kinetic property of the former. According to the Nyquist plots (Fig. S36), the comparison of charge transfer resistance for different catalysts agrees with the trend of acidic HER activity. The intrinsic activities of catalysts were further reflected by turnover frequency (TOF) value. The TOF of bimetallic (Fe$_{SA}$/Co$_{SA}$/Ni$_{SA}$)Ru$_{AC}$ are about an order of magnitude higher than that of Ru$_{AC}$@NCB at -0.05 V vs. RHE in both alkaline and acidic media (Fig. S37), highlighting the significantly higher catalytic activity of bimetallic M$_{SA}$Ru$_{AC}$ as compared to monometallic Ru$_{AC}$.

The pragmatic evaluation of $M_{SA}Ru_{AC}$@NCB for practical HER were conducted at industrial-level current densities (Fig. 5c, d). Remarkably, the optimal $M_{SA}Ru_{AC}$@NCB catalyst can readily reach high current densities of 1.2 A cm^{-2} at low overpotentials of 188 and 210 mV in alkaline and acidic media, respectively. Commercial Pt/C failed to work at such high current density in both alkaline and acidic media given the exaggerated overpotential required. Per Fig. S38, all $M_{SA}Ru_{AC}$@NCB catalysts demonstrate much higher mass activities than that of commercial Pt/C, which suggests the great potential for $M_{SA}Ru_{AC}$@NCB as highly cost-effective catalysts. Figure 5e and f compare the overpotentials of $M_{SA}Ru_{AC}$@NCB at 10 and 1000 mA cm^{-2} (η_{10} and η_{1000}) to the state-of-the-art electrocatalysts in previously published literatures, respectively. The pH-universal catalysts that were reported working at high current density is quite rare by far (Tables S6, 7). Among them, $M_{SA}Ru_{AC}$@NCB deliver the lowest η_{10} and η_{1000}, suggesting the superiority of $M_{SA}Ru_{AC}$@NCB for pH-universal HER electrocatalysis.

Long-term chronopotentiometry tests were performed to evaluate the catalytic durability. As demonstrated in Fig. S39, the potentials of $M_{SA}Ru_{AC}$@NCB remained stable after 100 hours operation at 10 mA cm^{-2}. The increases in potentials are only 21 mV for $Co_{SA}Ru_{AC}$@NCB in 0.5 M H_2SO_4 and 48 mV for $Ni_{SA}Ru_{AC}$@NCB in 1.0 M KOH during 100 h. In contrast, the potentials of Ru_{AC}@NCB baseline significantly increased by 64 and 120 mV in alkaline and acid media in only 50 hours. This result strongly proves the critical role of the interaction between M_{SA} and Ru_{AC} in stabilizing the structure of the active sites and maintaining the high HER activity.

The application potentials of $M_{SA}Ru_{AC}$@NCB were further verified in practical alkaline water electrolyzer (AWE), proton exchange membrane water electrolyzer (PEMWE) and anion exchange membrane water electrolyzer (AEMWE). The AWE employed $Co_{SA}Ru_{AC}$@NCB cathode and commercial RuO_2 anode (Fig. S40) needs a cell voltage of 1.63 V to achieve 500 mA cm^{-2} and 2.07 V to achieve 2 A cm^{-2} at 25 °C (Fig. 5g). At an elevated temperature of 55 °C, industrial level current densities of 2.2 A cm^{-2} and 3.7 A cm^{-2} can be obtained at 2 V and 2.25 V, respectively (Fig. 5g). The performance is among the highest compared to Pt/C anode based counterpart and other previously reported AWE devices (Table S8). Per Fig. 5h, the PEMWE for simulating industrial condition of acidic water electrolysis employing $Ni_{SA}Ru_{AC}$@NCB cathode and IrO_2 anode (Fig. S41) displays current densities of 1 A cm^{-2} at 2 V (25 °C) and 2.5 A cm^{-2} at 2.4 V (55 °C). Both electrolyzers demonstrate excellent catalytic durability, which delivered slow degradation for up to 350 hours (Figs. S42, 43). The $Co_{SA}Ru_{AC}$@NCB based AEMWE (Fig. S44) exhibits much lower voltage polarization as compared to commercial Pt/C based device (Fig. S45). Remarkably, the AEMWE electrolyzer can operate stably at industrial-level current density of 1 A cm^{-2} for 1000 hours (Fig. 5i).

Electrocatalysis mechanisms derived from $M_{SA}Ru_{AC}$ composites

DFT calculations were performed to understand the underlying electrocatalytic mechanism. The first step is to determine the true active sites in $M_{SA}Ru_{AC}$ composites. For alkaline HER, the H_2O adsorption is the primary decisive step because the proton supply is mainly from the H_2O dissociation in alkaline medium[54]. Therefore, the active site should be the position in the $M_{SA}Ru_{AC}$ composite that has the strongest adsorption towards H_2O. According to Fig. 6a, the H_2O adsorption energy on Ru_{AC} sites for all $M_{SA}Ru_{AC}$ composites are distinctly higher than those on $Fe_{SA}/Co_{SA}/Ni_{SA}$ sites (atomic coordinates of models listed in Supplementary Data 1). Therefore, Ru_{AC} should be the active sites (Fig. 6b). Figures 6c and S46 demonstrate the steric position of the alkaline HER active site, as well as the pronounced charge transfer between the H_2O adsorbate and the active site. Regarding to the active site in acidic medium, the adsorption of both H and H_2O should be considered. According to the calculated adsorption energies in Figs. 6a and S47, the H adsorption on $Fe_{SA}/Co_{SA}/Ni_{SA}$ sites are stronger than the H adsorption on Ru_{AC} sites. In addition, the H adsorption is much stronger than the H_2O adsorption on $Fe_{SA}/Co_{SA}/Ni_{SA}$, which greatly accelerate proton supply to the M_{SA} site. Therefore, the active site for acidic HER should be on the $Fe_{SA}/Co_{SA}/Ni_{SA}$ species. Figures 6c and S48 exhibit the configuration of H adsorbed active site and corresponding differential charge density.

Combining the experimental observation and theoretical calculation, the scenario of alkaline/acidic HER on $M_{SA}Ru_{AC}$ composites is demonstrated in Fig. 6d. Due to the different adsorption capabilities towards H_2O and H, the $M_{SA}Ru_{AC}$ composites have dual catalytic active sites, which is ascribed to M_{SA} and Ru_{AC} in acidic and alkaline solutions. The decoupling of active sites enables $M_{SA}Ru_{AC}$@NCB performing well for both acidic and alkaline HER. Moreover, the intrinsic electronic interaction between the symbiotic M_{SA} and Ru_{AC} generates inter-site synergy effect on the hydrogen evolution kinetics enhancement, which endows the bimetallic composites with far superior acidic/alkaline HER activity and durability than monometallic SA or AC.

On the basis of the active sites identification, the diverse structure-property relationships should be further established. For alkaline HER, the catalysts follow the order of $Co_{SA}Ru_{AC}$@NCB>$Ni_{SA}Ru_{AC}$@NCB>$Fe_{SA}Ru_{AC}$@NCB in terms of both η_{10} and mass activity (Fig. S49a). Whereas in 0.5 M H_2SO_4, the HER performance rank becomes $Ni_{SA}Ru_{AC}$@NCB>$Fe_{SA}Ru_{AC}$@NCB>$Co_{SA}Ru_{AC}$@NCB (Fig. S49b). This phenomenon is expected considering the decoupled active sites in different pH solutions and the different HER reaction pathways. According to Fig. 6e, all $M_{SA}Ru_{AC}$@NCB catalysts are energetically favorable for H_2O adsorption and dissociation processes during alkaline HER (Volmer step). The OH^- desorption is endothermic for all $M_{SA}Ru_{AC}$@NCB catalysts and identified as the rate-determining step (RDS). In-situ attenuated total reflection surface-enhanced infrared absorption spectroscopy (ATR-SEIRAS) shown in Fig. S50 experimentally verified the OH^- desorption as RDS. Basically, the facile OH^- desorption kinetics under alkaline environment alleviates the site poison caused by the strong OH^- adsorption and guarantees fresh active sites for continuous HER catalysis. As shown in Fig. 6g, the decrease of OH^- desorption energy barrier agrees well with the trend of η_{10} decease. In especial, $Co_{SA}Ru_{AC}$@NCB delivered the lowest energy barrier (0.556 eV) in this RDS, which endows $Co_{SA}Ru_{AC}$@NCB with the exceptionally low η_{10} of 8 mV. As for the acidic HER, a moderate ΔG_{H^*} close to 0 eV is desired[55–57]. $Ni_{SA}Ru_{AC}$@NCB exhibits the most desirable ΔG_{H^*} of -0.33 eV, which is more favorable than that of $Fe_{SA}Ru_{AC}$@NCB (−0.53 eV) and $Co_{SA}Ru_{AC}$@NCB (−0.68 eV) (Fig. 6f). Moreover, the acidic HER activities (η_{10}) of $M_{SA}Ru_{AC}$@NCB catalysts present a good linear relationship with the calculated ΔG_{H^*}, which matches well with the Sabatier principle (Fig. 6h)[57,58].

As demonstrated in Fig. 6i, under the principle of cohesive energy discrepancy driving SA/AC symbiosis, the library of atomically dispersed multimetallic materials can be further expanded. Benefited from the excellent universality, our synthesis methodology has significant potentials of expansion to other various electrocatalytic systems by designing and modulating the composition and configuration of atomically dispersed bi-/multi-metallic materials. Taking the bimetallic material as an example, for a target electrocatalytic reaction, metal element (M^1) with high intrinsic catalytic activity can be selected and $M^1_{SA/AC}$ specie can be constructed. During the symbiosis process, $M^2_{SA/AC}$ species with inherent interaction with $M^1_{SA/AC}$ can be simultaneously introduced, which can effectively modulate the electronic structure of $M^1_{SA/AC}$ and optimize the intermediate adsorption/desorption behavior thereby yielding the best catalytic performance. Moreover, the ultra-high flexibility of switching $M^2_{SA/AC}$ species is highly favorable for control experiment designing, providing excellent platforms for the electrocatalysis mechanism exploration.

To demonstrate the viability, we showcase additional three important electrocatalytic systems of alkaline oxygen reduction

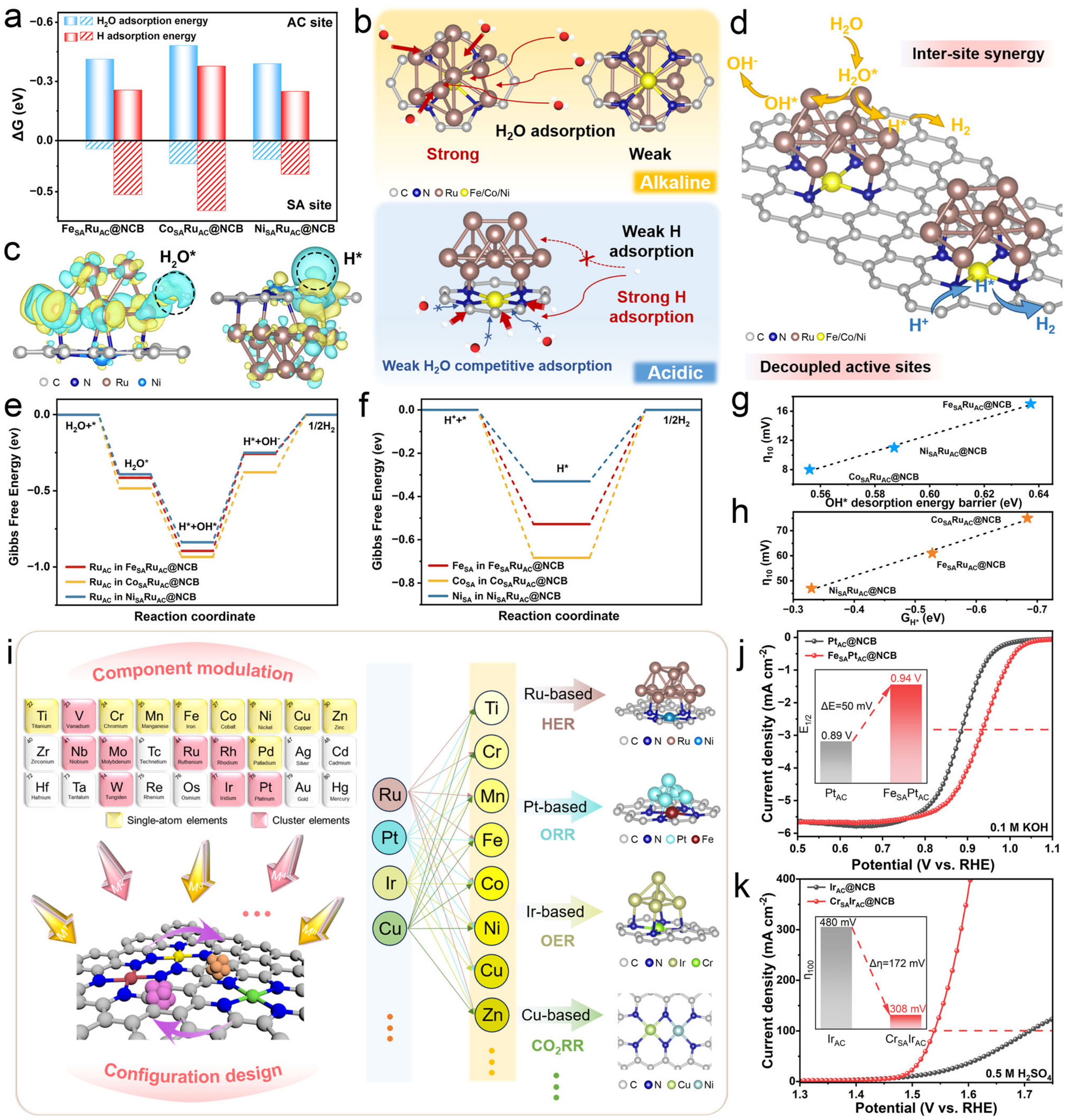

Fig. 6 | HER mechanism for $M_{SA}Ru_{AC}$@NCB and extensions of bimetallic materials in other electrocatalysis systems. **a** Comparison of H_2O and H adsorption energies. **b** Schematic of H_2O and H adsorption behaviors in alkaline and acidic media. **c** Differential charge density in $Ni_{SA}Ru_{AC}$@NCB model. **d** Schematic of the HER mechanism of $M_{SA}Ru_{AC}$@NCB. **e** Gibbs free energy diagrams for alkaline HER. **f** Gibbs free energy diagrams for acidic HER. **g** Relationship between η_{10} in alkaline HER and OH* desorption energy barrier. **h** Relationship between η_{10} in acidic HER and ΔG_{H^*}. **i** The principle of composition and configuration modulation towards SA/AC bimetallic sites for various electrocatalytic systems. **j** ORR polarization curves of $Fe_{SA}Pt_{AC}$@NCB and Pt_{AC}@NCB in 0.1 M KOH electrolyte. **k** OER polarization curves of $Cr_{SA}Ir_{AC}$@NCB and Ir_{AC}@NCB in 0.5 M H_2SO_4.

reaction (ORR), acidic oxygen evolution reaction (OER), and carbon dioxide reduction reaction (CO_2RR). For alkaline ORR, intrinsic high-active Pt was selected as the main element. Various secondary metal element was coupled with Pt clusters, yielding a set of $M_{SA}Pt_{AC}$@NCB materials (Fig. S51a). The M_{SA} species can effectively modulate the electronic structure of Pt_{AC}, as evidenced by the *d*-band center calculation results (Fig. S51b, c). As shown in Fig. 6j, we rapidly obtained the high-performance ORR catalyst of $Fe_{SA}Pt_{AC}$@NCB with the superior half-wave potential of 0.94 V. The ORR activities and *d*-band center of the catalysts exhibit classic volcano correlation with $Fe_{SA}Pt_{AC}$@NCB at the vertex (Fig. S52). An analogous strategy of catalyst development is also applicable for the acidic OER by conducting the control group of $M_{SA}Ir_{AC}$@NCB (Fig. S53). As demonstrated in Figs. 6k and S54, $Cr_{SA}Ir_{AC}$@NCB at the vertex of the volcano delivered the lowest η_{10} of 238 mV. Figures S55,56 and Tables S9, 10 displayed a comprehensive comparison of $Fe_{SA}Pt_{AC}$@NCB and $Cr_{SA}Ir_{AC}$@NCB with the state-of-the-art oxygen electrocatalysts, highlighting their leading positions of catalytic performances in the field. Regarding CO_2RR system, monatomic Cu_{SA} can be selected as the primary catalytically active species. The introduction of ancillary M_{SA} can significantly increase the CO production selectivity by 22.5 times comparing the performances of $Ni_{SA}Cu_{SA}$@NCB and Cu_{SA}@NCB (Fig. S57). The above results prove the great potential of our universal synthesis methodology for creating novel composite materials applied in extensive energy electrocatalysis areas.

Discussion

In summary, we develop a highly efficient and general methodology to synthesize a library of multimetallic single atom or/and atomic cluster composites. Because of the discrepancy in cohesive energy, multiple metal monomers follow energy-selective-clustering mechanism on nitrogen-functionalized carbon substrates, leading to the symbiosis of multimetallic single atoms or/and atomic clusters. Employing this mechanism, a total 40 types of bimetallic, trimetallic, quinary-metallic, and septenary-metallic SA/AC composites from 17 metal elements were constructed on NCB, including ultra-high loading septenary high-entropy single metal atom material that were barely synthesized in the field. The multimetallic SA/AC composites demonstrate great potential for electrocatalysis application. As a demonstrator, the model catalysts of $M_{SA}Ru_{AC}$@NCB exhibit superior electrocatalytic HER performances in both alkaline and acidic media and endow practical electrolyzers with top-level activity and durability. Controllable element modulations towards bimetallic $M^1{}_{SA}M^2{}_{AC}$@NCB created high-performance ORR and OER catalysts, which exemplified the significant potential of our synthesis methodology for versatile electrocatalysis systems. This work may inspire new researches for exploration and discovery of atomically dispersed metallic materials with ultra-complex elemental composition and mixing entropy.

Methods

Chemicals

Magnesium carbonate hydroxide pentahydrate ($C_4H_2Mg_5O_{14}\cdot 5H_2O$, 98%) was purchased from Alfa Aesar (China) Chemicals Co., Ltd. Potassium hydroxide (KOH, 95%), acetonitrile (C_2H_3N, 99.5%), bis(2,4-pentanedionato)manganese(II) ($C_{10}H_{14}MnO_4$, 99%), chromium(III) acetylacetonate ($C_{15}H_{21}CrO_6$, 99.99%), rhodium trichloride ($RhCl_3$, 98%), Ammoniumniobate(V)oxalatehydrate ($C_2H_5NNbO_4$, 98%) were purchased from Meryer Chemical Technology Co., Ltd. Ruthenium(III) chloride ($RuCl_3$, Ru 45-55%), vanadyl acetylacetonate ($C_{15}H_{21}O_6V$, 97%), titanium diisopropoxide bis(acetylacetonate) ($C_{16}H_{28}O_6Ti$), tungsten(VI) chloride (WCl_6, 99%), Iridium(III) chloride ($IrCl_3$, 99.8%), molybdenyl acetylacetonate ($C_{10}H_{14}MoO_6$, 97%), chloroplatinic acid hexahydrate were purchased from HEOWNS. Cobalt(II) chloride hexahydrate ($CoCl_2\cdot 6H_2O$, 99.99%), nickel(II) chloride hexahydrate ($NiCl_2\cdot 6H_2O$, 99.99%), iron(III) chloride hexahydrate ($FeCl_3\cdot 6H_2O$, 99%), copper(II) chloride dihydrate ($CuCl_2\cdot 2H_2O$, 99%), zinc chloride ($ZnCl_2$, 99.999%) and palladium(II) chloride ($PdCl_2$, 98%) were purchased from Macklin (Shanghai) Biochemical Technology Co., Ltd. Nafion was purchased from Sigma-Aldrich. Nickel foam (NF) was offered by Shanghai Keqi Technical Service Studio. Polyethersulfone (PES) membrane was obtained from Hangzhou Cobetter Filter Equipment Co., Ltd. Deionized water was used to prepare all solutions and electrolytes. Nafion 117 and Pt-coated Ti mesh substrate were purchased from Sinero. All chemicals are of analytical purity and used without further purification.

Synthesis of nitrogen-functionalized carbon nano box (NCB)

NCB was prepared by a chemical vapor deposition (CVD) method. In the typical synthesis process, 2.0 g $4MgCO_3\cdot Mg(OH)_2\cdot 5H_2O$ was placed in a porcelain boat and heated to 900 °C in a tube furnace with a heating rate of 5 °C min^{-1} under 60 sccm N_2 flow. A gas-washing bottle containing acetonitrile was connected in the N_2 up-stream and the flow rate was reduced to 20 sccm. The CVD process lasted for 3 h at 900 °C, and afterwards the gas-washing bottle was removed. The product powders were washed with 6 M HCl at room temperature for 24 h and dried in a blast oven at 60 °C to obtain nitrogen-functionalized carbon nanobox (NCB).

Synthesis of $M_{SA}Ru_{AC}$@NCB (M=Ni, Ti, Cr, Mn, Fe, Co, Cu, Zn, Pd)

In the typical synthesis process, 2.37 mg $NiCl_2\cdot 6H_2O$ (or 3.64 mg $C_{16}H_{28}O_6Ti$, 3.49 mg $C_{15}H_{21}CrO_6$, 2.53 mg $C_{10}H_{14}MnO_4$, 2.70 mg $FeCl_3\cdot 6H_2O$, 2.38 mg $CoCl_2\cdot 6H_2O$, 1.70 mg $CuCl_2\cdot 2H_2O$, 1.36 mg $ZnCl_2$, 1.77 mg $PdCl_2$), 4.14 mg $RuCl_3$ and 20 mg NCB were dissolved in 10 mL deionized water, and then stirred at room temperature for 24 h. The mixture was then filtered and freeze-dried. The obtained solid was calcined at 500 °C for 1 h under Ar atmosphere with a heating rate of 10 °C min^{-1}.

Synthesis of $M_{AC}Ru_{AC}$@NCB (M=V, Mo, Rh, W, Ir, Pt)

In the typical synthesis process, 2.65 mg $C_{10}H_{14}O_5V$ (or 3.26 mg $C_{10}H_{14}MoO_6$, 2.09 mg $RhCl_3$, 3.96 mg WCl_6, 2.98 mg $IrCl_3$, 5.17 mg H_2PtCl_6), 4.14 mg $RuCl_3$ and 20 mg NCB were dissolved in 10 mL deionized water and then stirred at room temperature for 24 h. The mixture was then filtered and freeze-dried. The obtained solid was calcined at 500 °C for 1 h under Ar atmosphere with a heating rate of 10 °C min^{-1}.

Synthesis of $Fe_{SA}Ni_{SA}$@NCB, $Co_{SA}Ni_{SA}$@NCB and $Ni_{SA}Pd_{SA}$@NCB

In the typical synthesis process, 2.37 mg $NiCl_2\cdot 6H_2O$, 2.70 mg $FeCl_3\cdot 6H_2O$ (or 2.38 mg $CoCl_2\cdot 6H_2O$, 2.37 mg $NiCl_2\cdot 6H_2O$, or 1.77 mg $PdCl_2$, 2.37 mg $NiCl_2\cdot 6H_2O$) and 20 mg NCB was dissolved in 10 mL deionized water and then stirred at room temperature for 24 h. The mixture was then filtered and freeze-dried. The obtained solid was calcined at 500 °C for 1 h under Ar atmosphere with a heating rate of 10 °C min^{-1}.

Synthesis of Ru_{AC}@NCB, Fe_{SA}@NCB, Co_{SA}@NCB, Ni_{SA}@NCB

The synthesis processes of Ru_{AC}@NCB and $Fe_{SA}/Co_{SA}/Ni_{SA}$@NCB specimens are similar to that of $Ni_{SA}Ru_{AC}$@NCB except that $RuCl_3$, $FeCl_3\cdot 6H_2O$, $CoCl_2\cdot 6H_2O$, $NiCl_2\cdot 6H_2O$ were not added.

Synthesis of $Fe_{SA}Co_{SA}Ni_{SA}$@NCB

2.70 mg $FeCl_3\cdot 6H_2O$, 2.38 mg $CoCl_2\cdot 6H_2O$, 2.37 mg $NiCl_2\cdot 6H_2O$, and 10 mg NCB were dissolved in 10 mL deionized water, and then stirred at room temperature for 24 h. The mixture was then filtered and freeze-dried. The obtained solid was calcined at 500 °C for 1 h under Ar atmosphere with a heating rate of 10 °C min^{-1}.

Synthesis of $Fe_{SA}Co_{SA}Ni_{SA}Cr_{SA}Mn_{SA}$@NCB

2.70 mg $FeCl_3\cdot 6H_2O$, 2.38 mg $CoCl_2\cdot 6H_2O$, 2.37 mg $NiCl_2\cdot 6H_2O$, 3.49 mg $C_{15}H_{21}CrO_6$, 2.53 mg $C_{10}H_{14}MnO_4$, and 10 mg NCB were dissolved in 10 mL deionized water, and then stirred at room temperature for 24 h. The mixture was then filtered and freeze-dried. The obtained solid was calcined at 500 °C for 1 h under Ar atmosphere with a heating rate of 10 °C min^{-1}.

Synthesis of $Fe_{SA}Co_{SA}Ni_{SA}Cr_{SA}Mn_{SA}Cu_{SA}Pd_{SA}$@NCB

2.70 mg $FeCl_3\cdot 6H_2O$, 2.38 mg $CoCl_2\cdot 6H_2O$, 2.37 mg $NiCl_2\cdot 6H_2O$, 3.49 mg $C_{15}H_{21}CrO_6$, 2.53 mg $C_{10}H_{14}MnO_4$, 1.70 mg $CuCl_2\cdot 2H_2O$, 1.77 mg $PdCl_2$, and 10 mg NCB were dissolved in 10 mL deionized water, and then stirred at room temperature for 24 h. The mixture was then filtered and freeze-dried. The obtained solid was calcined at 500 °C for 1 h under Ar atmosphere with a heating rate of 10 °C min^{-1}.

The syntheses of other bi-/multi-metallic atomically dispersed materials follow the same steps by using the appropriate metal precursor, heating rate, sintering time and sintering temperature (Table S2).

Material characterizations

Field emission scanning electron microscopy (SEM) measurement was conducted using a JSM-7800F from JEOL. Transmission electron microscopy (TEM) was conducted using a JEM-2100F from JEOL which operated at 200 kV. High-angle annular dark-field (HAADF)-STEM was conducted using a JEM-ARM200F from JEOL. The in-situ heating TEM was conducted using a JEM-ARM300F from JEOL. X-ray diffraction (XRD) was tested on a Bruker-D8 Advanced X-ray Diffractometer using Cu Kα radiation (λ = 0.15406 nm). XPS measurements were conducted using an X-ray photoelectron spectrometer (Axis Supra, Kratos). Inductively coupled plasma-mass spectrometry (ICP-MS) was conducted using Agilent 5110. X-ray absorption spectroscopy (XAS) spectra were performed in the Shanghai Synchrotron Radiation Facility (SSRF). The acquired X-ray absorption near-edge structure (XANES) and extended X-ray absorption fine structure (EXAFS) data were analyzed by the ATHENA module of the IFEFFIT software package[59]. The EXAFS fitting data was collected using the ARTEMIS module implemented in the IFEFFIT software package. The wavelet transforms (WT) were obtained by the Fortran-based HAMA code[60].

Electrochemical measurements

Electrochemical measurements of HER. Electrochemical performances were assessed via an electrochemical workstation (CHI660E, Shanghai, China) in a three-electrode cell system at room temperature. Catalyst-coated carbon cloth, graphite rod, and saturated calomel electrode (SCE) were used as working, counter and reference electrodes, respectively. The electrolytes employed are N_2-saturated 1 M KOH (pH = 13.7 ± 0.1) and 0.5 M H_2SO_4 (pH = 0.4 ± 0.1) aqueous solution for alkaline and acidic HER, respectively. The electrolyte is synthesized before the electrochemical testing and stored sealed at room temperature. The working electrodes were prepared as follows: uniform suspension containing 5 mg catalyst, 965 µL isopropyl alcohol, and 35 µL 5 wt% Nafion solution were obtained by ultrasonic mixing for about 30 min. Afterward, 200 µL catalyst ink was coated onto the 1 × 1 cm^2 carbon cloth, which was dried in air. The typical catalyst loading is 1 mg cm^{-2} on carbon cloth, yielding a noble metal mass loading of ca. 0.40 mg_{Ru} cm^{-2} loading for all samples. The potential measured is referenced to the reference electrode, necessitating conversion to the potential relative to the reversible hydrogen electrode (RHE). Platinum wire electrodes served as both the working and counter electrodes during calibration in an H_2-saturated electrolyte. The zero current potential was determined through cyclic voltammetry (CV) measurements.

$$E_{\mathrm{RHE}} = E_{\mathrm{SCE}} + E^{\theta}_{\mathrm{SCE}} + 0.059\mathrm{pH} \tag{1}$$

Cyclic voltammetry (CV) was conducted in the potential range of 0.168 to −0.532 V versus RHE at a sweep rate of 100 mV s^{-1} for 20 cycles for catalyst activation. Linear sweep voltammetry (LSV) was conducted in the same potential range of CV measurements at a scan rate of 5 mV s^{-1}. Tafel slope was calculated with according to the LSV profiles. CV was also performed in the scan rate range of 10 to 70 mV s^{-1} to calculate the double-layer capacitance (C_{dl}). Electrochemical impedance spectroscopy (EIS) was tested by applying an AC voltage with 5 mV amplitude in a frequency range from 100 KHz to 0.01 Hz. For the durability evaluation, the chronopotentiometry were obtained with a constant current density of 10 mA cm^{-2}. Each data has undergone repeatability testing, mitigating sources of random error through stringent test specifications. The data demonstrate high accuracy and reproducibility, falling within experimental error margins. All measurements were performed without iR compensation if not explicitly specified.

Electrochemical measurements in the AWE device

Electrochemical performances for practical alkaline water splitting were tested in the zero-gap alkaline water electrolyzer (AWE). The electrochemical measurements were performed on the IV2010 DC power supply. The prepared $Co_{SA}Ru_{AC}$@NCB and commercial RuO_2 catalysts were used as cathode and anode with a loading of 1 mg cm^{-2}. The mass loading of Ru on the cathode and anode is approximately 0.4 and 0.76 mg_{Ru} cm^{-2}, respectively. For comparison, noble metal catalysts Pt/C and RuO_2 were also used as cathode and anode under the same conditions. The mass loading of Pt on the cathode is approximately 0.20 mg_{Pt} cm^{-2}, and the mass loading of Ru on the cathode is approximately 0.76 mg_{Ru} cm^{-2}. To prepare the anode and cathode ink, catalysts were dispersed to a mixture of isopropanol and distilled water. Then, Nafion® solution (5 wt%) was added. After ultrasonicated for at least 1 h in a low-temperature water bath, a uniform catalyst ink can be obtained. Porous polyethersulfone (PES) has a thickness of 0.12 mm and the pore diameter is 0.22 µm, which was used as the separator. The active area of the electrode is measured to be 1×1 cm^2. 6 M KOH solution was used as both anolyte and catholyte. The circulation of the electrolyte was enabled by the peristaltic pump at 80 rpm and the inner diameter of the hose was 3 mm. No iR compensation was applied. For the activity evaluation, polarization curves were obtained at 25 °C and 55 °C. For the durability evaluation, the chronopotentiometric curves were obtained with a constant current density of 1.5 A cm^{-2} at 25 °C.

Electrochemical measurements in the AEMWE device

Electrochemical performances for practical alkaline water splitting were tested in an anion exchange membrane water electrolyzer (AEMWE). The electrochemical measurements were performed on the IV2010 DC power supply. The prepared slurries of the cathodic and anodic catalysts were firstly air-sprayed onto porous carbon paper and Ni foam gas diffusion layers (GDLs), respectively. Subsequently, the catalyst-coated GDLs were pressed with an anion exchange membrane (Fuma® FAA-3-50, thickness 130µm) to assemble into the membrane electrode assembly (MEA). The active area of the electrode is measured to be 1 × 1 cm^2. The mass loading of Ru on the cathode and anode is ca 0.40 and 0.76 mg_{Ru} cm^{-2}, respectively. Note that except for catalysts, other experimental conditions including the assembly techniques of the device and the testing parameters kept identical. The anion exchange membrane was immersed into 1 M KOH solution for at least 24 h prior to being used to exchange Cl^- into OH^-. 1 M KOH solution was used as both anolyte and catholyte. For the activity evaluation, polarization curves were obtained at 25 °C. The stability of the AEMWE was evaluated by chronopotentiometry test at a current density of 1 A cm^{-2} at a water temperature of 25 °C.

Electrochemical measurements in the PEMWE device

For the PEMWE, home-made IrO_2 was used as the anode catalyst for the oxygen evolution reaction (OER) and $Ni_{SA}Ru_{AC}$@NCB was used as the cathode HER catalyst. Nafion 117 served as the cation exchange membrane (DuPont, thickness 183 µm, N117). The catalyst inks were directly air-sprayed on both sides of the Nafion 117 membrane, with an IrO_2 loading of 2 mg cm^{-2} (1.71 mg_{Ir} cm^{-2}) for the anode and a $Ni_{SA}Ru_{AC}$@NCB loading of 1 mg cm^{-2} (0.40 mg_{Ru} cm^{-2}) for the cathode. The titanium felt with a thickness of 0.25 mm were used as gas diffusion layers in both the anode and cathode. The resulting CCMs were then pressed between the anode and cathode GDLs to form the MEA. The active area of the electrode is measured to be 1 × 1 cm^2. During measurement, water was continuously pumped through the PEMWE. All voltages measured in PEMWEs were obtained without iR correction. The electrochemical measurements were performed on the IV2010 DC power supply.

The calculation for turnover frequency (TOF)

The TOF value was calculated based on the estimated number of active sites:

$$\mathrm{TOF} = \frac{\text{Number of hydrogen turnover}}{\text{Number of active sites}} \tag{2}$$

$$\text{Number of hydrogen turnover(mol/s)} = \frac{\mathrm{j(A)}}{2\mathrm{F}} \tag{3}$$

Where j is current, the number 2 means two electrons per mol of H_2 evolution, and F is a Faraday constant of 96,485.3 C. We assume that all Ru atoms in the catalysts are active for HER. The numbers of Ru atoms number in Ru_{AC}@NCB and $M_{SA}Ru_{AC}$@NCB catalysts were calculated from the Ru molar mass and the mass loading on the carbon cloth. The weight contents of various metals in the catalysts were determined by ICP-MS as shown in Table S5.

Calculation Method

All the calculations were performed using the density functional theory (DFT) within the Vienna Ab initio Software Package (VASP 5.4.4) code, employing the Perdew–Burke–Ernzerhof (PBE) generalized gradient approximation and the projected augmented wave (PAW) method[61–64]. The cutoff energy of the plane-wave was fixed at 400 eV. Electronic self-consistent iterations were set with a force of 10^{-5} eV and 0.01 eV/Å. To prevent interactions between periodic images, a 15 Å vacuum layer was added. During the model construction process, we selected Ru_{10} clusters and placed them on the modified carbon-based substrate $Fe_{SA}/Co_{SA}/Ni_{SA}$-N_4. The Brillouin zone of the surface unit cell was performed with 3 × 3 × 1 Monkhorst–Pack grid varying k-point sampling for catalyst optimizations[65].

For calculations of isolated metal atoms in a vacuum, a 9 × 10 × 11 Å broken symmetry cell was utilized to guarantee the correct occupancy of degenerate orbitals. All theoretical calculations were non-spin-polarized, except for the isolated metal atom calculations and magnetic Fe, Ni, Mn, and Co. Cohesive energy (E_c) is represented as the energy variation per atom according to the following formula:

$$E_c = \frac{E_{\mathrm{bulk}}}{N} - E_{\mathrm{at}} \tag{4}$$

where E_{at} represents the energy of the isolated metal atom within a vacuum, E_{bulk} signifies the energy of the bulk unit cell comprising N atoms.

The adsorption energy (E_{ads}) of the surface species is determined by

$$E_{\mathrm{ads}} = E_{\mathrm{total}} - E_{\mathrm{surface}} - E_{\mathrm{species}} \tag{5}$$

where E_{total} denotes the overall energy of the adsorbed species in conjunction with the catalyst surface, E_{surface} signifies the energy of the bare surface, and E_{species} represents the energy of the species in the gaseous phase.

The binding energy (E_b) is determined by:

$$E_b = E_{AB} - E_A - E_B \tag{6}$$

where E_{AB} stands for the total energy of the adsorption structure involving the entire metal solvation, E_A refers to the energy of metal-solvated structures within an empty crystal, and E_B indicates the energy of the substrate.

The free energies of adsorbates at 298.15 K were estimated according to the harmonic approximation. The entropy was determined by applying the following equation:

$$S(T) = k_B \sum_{i}^{\text{harm DOF}} \left[\frac{\varepsilon_i}{k_B T \left(e^{\varepsilon_i/k_B T} - 1 \right)} - \ln\left(1 - e^{-\varepsilon_i/k_B T} \right) \right] \tag{7}$$

where k_B is Boltzmann's constant; DOF is the number of harmonic energies (ε_i) considered in the summation. The free energies of gas phase species are adjusted as follows:

$$G_g(T) = E_{\mathrm{elec}} + E_{\mathrm{ZPE}} + \int C_P \, dt - TS(T) \tag{8}$$

Where C_P is the specific heat capacity of a gas. The parameters are acquired from the NIST database (https://doi.org/10.18434/T4D303). We employed 0.035 bar of gas-phase water as the benchmark reference state for water due to its equilibrium with liquid water at 300 K under this specific pressure condition[66,67].

Ab initio molecular dynamics (AIMD) simulation

AIMD simulations based on geometrically optimized structures were conducted at 298.15 K with a time step of 1 fs. The Nose-Hoover thermostat was employed to maintain a constant temperature. Following continuous 10 ps AIMD simulations, thermodynamically stable states were achieved.

Data availability

The relevant data generated in this study are provided in the Supplementary Information. Source data are provided with this paper.

References

1. Chong, L. et al. La- and Mn-doped cobalt spinel oxygen evolution catalyst for proton exchange membrane electrolysis. *Science* **380**, 609–616 (2023).
2. Han, L. et al. A single-atom library for guided monometallic and concentration-complex multimetallic designs. *Nat. Mater.* **21**, 681–688 (2022).
3. Gu, J. et al. Synergizing metal–support interactions and spatial confinement boosts dynamics of atomic nickel for hydrogenations. *Nat. Nanotechnol.* **16**, 1141–1149 (2021).
4. Sun, T. et al. Ferromagnetic single-atom spin catalyst for boosting water splitting. *Nat. Nanotechnol.* **18**, 763–771 (2023).
5. Yao, Y. et al. High-entropy nanoparticles: Synthesis-structure-property relationships and data-driven discovery. *Science* **376**, eabn3103 (2022).
6. Zhang, X. et al. A stable low-temperature H2-production catalyst by crowding Pt on α-MoC. *Nature* **589**, 396–401 (2021).
7. Li, X. et al. Advances in heterogeneous single-cluster catalysis. *Nat. Rev. Chem.* **7**, 754–767 (2023).
8. Ni, W. Y. et al. Synergistic interactions between PtRu catalyst and nitrogen-doped carbon support boost hydrogen oxidation. *Nat. Catal.* **6**, 773–783 (2023).
9. Xiao, F. et al. Atomically dispersed Pt and Fe sites and Pt–Fe nanoparticles for durable proton exchange membrane fuel cells. *Nat. Catal.* **5**, 503–512 (2022).
10. Yan, H. et al. Bottom-up precise synthesis of stable platinum dimers on graphene. *Nat. Commun.* **8**, 1070 (2017).
11. Zhang, J. K. et al. Mechanistic insight into the synergy between platinum single atom and cluster dual active sites boosting photocatalytic hydrogen evolution. *Adv. Mater.* **35**, 2300902 (2023).
12. Hai, X. et al. Geminal-atom catalysis for cross-coupling. *Nature* **622**, 754–760 (2023).
13. Xie, F. X. et al. A general approach to 3D-printed single-atom catalysts. *Nat. Synth.* **2**, 129–139 (2023).

14. Wang, Q. et al. Atomic metal–non-metal catalytic pair drives efficient hydrogen oxidation catalysis in fuel cells. *Nat. Catal.* **6**, 916–926 (2023).
15. Gao, Q. et al. Synthesis of core/shell nanocrystals with ordered intermetallic single-atom alloy layers for nitrate electroreduction to ammonia. *Nat. Synth.* **2**, 624–634 (2023).
16. Poerwoprajitno, A. R. et al. A single-Pt-atom-on-Ru-nanoparticle electrocatalyst for CO-resilient methanol oxidation. *Nat. Catal.* **5**, 231–237 (2022).
17. Chang, X. et al. Designing single-site alloy catalysts using a degree-of-isolation descriptor. *Nat. Nanotechnol.* **18**, 611–616 (2023).
18. Jiao, F. et al. Disentangling the activity-selectivity trade-off in catalytic conversion of syngas to light olefins. *Science* **380**, 727–730 (2023).
19. Wei, Y. M., Ma, X. D., Wang, M. F. & Duan, X. F. Synergism of Fe/Ti enabled regioselective arene Difunctionalization. *J. Am. Chem. Soc.* **145**, 1542–1547 (2023).
20. Lin, X. X., Hong, J. F., Wang, C. C., Su, M. X. & Zhou, S. F. CoZnO/C@BCN nanocomposites derived from bimetallic hybrid ZIFs for enhanced electromagnetic wave absorption. *J. Mater. Chem. A* **11**, 17737–17747 (2023).
21. Zhou, M. et al. Photocatalytic CO_2 reduction using La-Ni bimetallic sites within a covalent organic framework. *Nat. Commun.* **14**, 2473 (2023).
22. Li, Q. et al. Pressure-induced optical transitions in metal nanoclusters. *ACS Nano* **14**, 11888–11896 (2020).
23. Huang, W. et al. Ultrahigh density of atomic CoFe-Electron synergy in noncontinuous carbon matrix for highly efficient magnetic wave adsorption. *Nano-Micro Lett.* **14**, 96 (2022).
24. Dong, C. et al. Dual-functional single-atomic Mo/Fe clusters–decorated C3N5 via three electron-pathway in oxygen reduction reaction for tandemly removing contaminants from water. *Proc. Natl Acad. Sci.* **120**, e2305883120 (2023).
25. Chen, Z. et al. Single-atom Mo-Co catalyst with low biotoxicity for sustainable degradation of high-ionization-potential organic pollutants. *Proc. Natl Acad. Sci.* **120**, e2305933120 (2023).
26. Li, R. et al. Polystyrene Waste Thermochemical Hydrogenation to Ethylbenzene by a N-bridged Co, Ni dual-atom catalyst. *J. Am. Chem. Soc.* **145**, 16218–16227 (2023).
27. Fang, C. et al. Synergy of dual-atom catalysts deviated from the scaling relationship for oxygen evolution reaction. *Nat. Commun.* **14**, 4449 (2023).
28. Li, H. et al. Bimetallic diatomic nanoclusters with longitudinal Fe–O–Fe units and latitudinal Cu–S–Fe–S–Cu units as efficient ORR active sites. *J. Mater. Chem. A* **10**, 14828–14837 (2022).
29. Hai, X. et al. Scalable two-step annealing method for preparing ultra-high-density single-atom catalyst libraries. *Nat. Nanotechnol.* **17**, 331–331 (2022).
30. Liu, H. et al. Decorating single-atomic Mn sites with FeMn clusters to boost oxygen reduction reaction. *Angew. Chem. Int. Ed.* **62**, e202214988 (2023).
31. Wei, X. Q. et al. Tuning the spin state of Fe single atoms by Pd nanoclusters enables robust oxygen reduction with dissociative pathway. *Chem* **9**, 181–197 (2023).
32. Abe, J. O., Popoola, A. P. I., Ajenifuja, E. & Popoola, O. M. Hydrogen energy, economy and storage: Review and recommendation. *Int. J. Hydrog. Energy* **44**, 15072–15086 (2019).
33. Zou, X. & Zhang, Y. Noble metal-free hydrogen evolution catalysts for water splitting. *Chem. Soc. Rev.* **44**, 5148–5180 (2015).
34. Sun, L., Reddu, V. & Wang, X. Multi-atom cluster catalysts for efficient electrocatalysis. *Chem. Soc. Rev.* **51**, 8923–8956 (2022).
35. Rong, H., Ji, S., Zhang, J., Wang, D. & Li, Y. Synthetic strategies of supported atomic clusters for heterogeneous catalysis. *Nat. Commun.* **11**, 5884 (2020).
36. Li, Z., Li, B. & Li, Q. Single-Atom Nano-Islands (SANIs): A robust atomic-nano system for versatile heterogeneous catalysis applications. *Adv. Mater.* **35**, e2211103 (2023).
37. Su, Y. Q. et al. Stability of heterogeneous single-atom catalysts: a scaling law mapping thermodynamics to kinetics. *Npj Comput. Mater.* **6**, 144 (2020).
38. Esposito, D. V., Hunt, S. T., Kimmel, Y. C. & Chen, J. G. A new class of electrocatalysts for hydrogen production from water electrolysis: metal monolayers supported on low-cost transition metal carbides. *J. Am. Chem. Soc.* **134**, 3025–3033 (2012).
39. Zhu, C., Fu, S., Shi, Q., Du, D. & Lin, Y. Single-atom electrocatalysts. *Angew. Chem. Int. Ed.* **56**, 13944–13960 (2017).
40. Wu, L. P., Guo, T. & Li, T. Rational design of transition metal single-atom electrocatalysts: a simulation-based, machine learning-accelerated study. *J. Mater. Chem. A* **8**, 19290–19299 (2020).
41. Wang, A. Q., Li, J. & Zhang, T. Heterogeneous single-atom catalysis. *Nat. Rev. Chem.* **2**, 65–81 (2018).
42. Tang, S. et al. Realizing a not-strong-not-weak polarization electric field in single-atom catalysts sandwiched by Boron nitride and graphene sheets for efficient nitrogen fixation. *J. Am. Chem. Soc.* **142**, 19308–19315 (2020).
43. Ha, M. et al. Tuning metal single atoms embedded in NxCy moieties toward high-performance electrocatalysis. *Energy Environ. Sci.* **14**, 3455–3468 (2021).
44. Oschinski, H., Morales-García, Á. & Illas, F. Interaction of first row transition metals with M2C (M = Ti, Zr, Hf, V, Nb, Ta, Cr, Mo, and W) MXenes: A quest for single-atom catalysts. *J. Phys. Chem. C.* **125**, 2477–2484 (2021).
45. Üzengi Aktürk, O., Aktürk, E. & Ciraci, S. Effects of adatoms and physisorbed molecules on the physical properties of antimonene. *Phys. Rev. B* **93**, 035450 (2016).
46. Zhu, Z. et al. High-capacity, cooperative CO_2 capture in a Diamine-appended metal–organic framework through a combined chemisorptive and physisorptive mechanism. *JACS* **146**, 6072–6083 (2024).
47. Kittel C. McEuen P. *Introduction to solid state physics*. John Wiley & Sons (2018).
48. Lei, X. et al. High-entropy single-atom activated carbon catalysts for sustainable oxygen electrocatalysis. *Nat. Sustain.* **6**, 816–826 (2023).
49. Rao, P. et al. Movable type printing method to synthesize high-entropy single-atom catalysts. *Nat. Commun.* **13**, 5071 (2022).
50. Yao, Y. et al. Engineering the electronic structure of single atom Ru sites via compressive strain boosts acidic water oxidation electrocatalysis. *Nat. Catal.* **2**, 304–313 (2019).
51. Hai, X. et al. Engineering local and global structures of single Co atoms for a superior oxygen reduction reaction. *ACS Catal.* **10**, 5862–5870 (2020).
52. Yang, J. et al. Efficient and robust hydrogen evolution: phosphorus nitride imide nanotubes as supports for anchoring single ruthenium sites. *Angew. Chem. Int. Ed.* **57**, 9495–9500 (2018).
53. Yu, J. et al. Recent advances and prospective in Ruthenium-based materials for electrochemical water splitting. *ACS Catal.* **9**, 9973–10011 (2019).
54. Mahmood, J. et al. An efficient and pH-universal ruthenium-based catalyst for the hydrogen evolution reaction. *Nat. Nanotechnol.* **12**, 441–446 (2017).
55. Sun, Y. et al. Modulating electronic structure of metal-organic frameworks by introducing atomically dispersed Ru for efficient hydrogen evolution. *Nat. Commun.* **12**, 1369 (2021).
56. Norskov, J. K., Bligaard, T., Rossmeisl, J. & Christensen, C. H. Towards the computational design of solid catalysts. *Nat. Chem.* **1**, 37–46 (2009).

57. Medford, A. J. et al. From the Sabatier principle to a predictive theory of transition-metal heterogeneous catalysis. *J. Catal.* **328**, 36–42 (2015).
58. Logadottir, A. et al. The Brønsted–Evans–Polanyi relation and the volcano plot for ammonia synthesis over transition metal catalysts. *J. Catal.* **197**, 229–231 (2001).
59. Ravel, B. & Newville, M. ATHENA, ARTEMIS, HEPHAESTUS: data analysis for X-ray absorption spectroscopy using IFEFFIT. *J. Synchrotron Radiat.* **12**, 537–541 (2005).
60. Timoshenko, J. & Kuzmin, A. Wavelet data analysis of EXAFS spectra. *Comput. Phys. Commun.* **180**, 920–925 (2009).
61. Perdew, J. P., Burke, K. & Ernzerhof, M. Generalized gradient approximation made simple. *Phys. Rev. Lett.* **77**, 3865–3868 (1996).
62. Hammer, B., Hansen, L. B. & Nørskov, J. K. Improved adsorption energetics within density-functional theory using revised Perdew-Burke-Ernzerhof functionals. *Phys. Rev. B* **59**, 7413–7421 (1999).
63. Blöchl, P. E. Projector augmented-wave method. *Phys. Rev. B* **50**, 17953–17979 (1994).
64. Kresse, G. & Joubert, D. From ultrasoft pseudopotentials to the projector augmented-wave method. *Phys. Rev. B* **59**, 1758–1775 (1999).
65. Monkhorst, H. J. & Pack, J. D. Special points for Brillouin-zone integrations. *Phys. Rev. B* **13**, 5188–5192 (1976).
66. Rossmeisl, J., Logadottir, A. & Norskov, J. K. Electrolysis of water on (oxidized) metal surfaces. *Chem. Phys.* **319**, 178–184 (2005).
67. Weast RC. CRC handbook of chemistry and physics. (1986).

Acknowledgements

We acknowledge financial support from the National Natural Science Foundation of China (Nos. 52122107, 52072257, 52372218, U22A20119).

Author contributions

X.H., J.D., and W.H. conceived the project. X.Y. and W.S. designed the experiments. X.Y., X.Y.W., Y.C., and N.Y. performed data analysis and experiments discussions. X.Y. and X.W. participated in the XAFS experiments and data analyses. X.Y., W.S., and J.Z. conducted HAADF-STEM and HRTEM measurements and data analyses. H.W. and K.L. carried out the DFT simulations. X.Y., X.H., and J.D. wrote the paper. All authors discussed the results and commented on the manuscript.

Competing interests

The authors declare no competing interests.

Additional information

Supplementary information The online version contains supplementary material available at https://doi.org/10.1038/s41467-024-52520-1.

Correspondence and requests for materials should be addressed to Xiaopeng Han or Jia Ding.

Peer review information *Nature Communications* thanks Jiong Lu, Pranab Sarkar, and the other, anonymous, reviewer(s) for their contribution to the peer review of this work. A peer review file is available.

Reprints and permissions information is available at http://www.nature.com/reprints